

Unsteady Aerodynamics of a Morphing Tandem-Wing Unmanned Aerial Vehicle

G. Q. Zhang* and S. C. M. Yu†

Nanyang Technological University, Singapore 639798, Republic of Singapore

DOI: 10.2514/1.C031652

The effects of unsteady aerodynamics for a tandem-wing unmanned aerial vehicle (UAV) prototype during the morphing stage have been investigated numerically at low Reynolds numbers ($Re < 10^6$). The morphing stage consists of two stages. The first stage involves the unfolding of the canards and wings from their initial position in which they were attached and aligned parallel to the UAV fuselage. The second stage involves the rotation of the unfolded canards and wings around the chord axis toward their final orientations. Lift and drag coefficients for the canard and wing vary significantly, particularly during the second morphing stage. Maximum deviation can be 2 to 14 times higher than the final steady state values. A significant increase in the hinge moment is also observed during the first morphing stage but the sign of the moment remains the same throughout. The unsteady aerodynamics, however, have larger effects during the second morphing stage, including the rapid change in the sign for the hinge moment, the corresponding magnitude also differs by (+) 57% and (+) 260% for the canard and wing, respectively. Attempts have been made to correlate these observations with the vortex interactions between the canard and wing during the morphing process.

Nomenclature

c	= chord length, m
C_d	= drag coefficient
C_L	= lift coefficient
C_P	= pressure coefficient
F	= damping
G	= vertical distance between the canard and wing (with respect to c)
M	= hinge moment
Re	= Reynolds number, Uc/γ
St	= longitudinal separation of the canard and wing, stagger (with respect to c)
T	= total unfolded time
U	= freestream velocity
α	= angle of attack
γ	= kinematic viscosity of the freestream fluid
δ_{XC}	= canard deflection angle at x -axis
δ_{XW}	= wing deflection angle at x -axis
δ_{YC}	= canard deflection angle at y -axis
δ_{YW}	= wing deflection angle at y -axis
ζ	= vorticity

Subscripts

d	= downstroke
u	= upstroke

I. Introduction

MORPHING aircrafts are flight vehicles that can change their shape so as to achieve better performance at different flight conditions. The NASA morphing project defines morphing as an efficient multipoint adaptability that includes macro, micro,

Received 6 September 2011; revision received 25 April 2012; accepted for publication 27 April 2012. Copyright © 2012 by the American Institute of Aeronautics and Astronautics, Inc. All rights reserved. Copies of this paper may be made for personal or internal use, on condition that the copier pay the \$10.00 per-copy fee to the Copyright Clearance Center, Inc., 222 Rosewood Drive, Danvers, MA 01923; include the code 0021-8669/12 and \$10.00 in correspondence with the CCC.

*Research Fellow, Aerospace Engineering Division, School of Mechanical and Aerospace Engineering; zhangguoqing@ntu.edu.sg. Corresponding Author.

†Associate Professor, Aerospace Engineering Division, School of Mechanical and Aerospace Engineering.

structural, and/or fluidic approaches [1]. The Defense Advanced Research Projects Agency also defines morphing as a platform that is able to change its shape substantially (approximately 50% or more) to adapt to a changing environment, making the vehicle flight performance better in the new environment than before the change [2].

The recent advances in the unmanned aerial vehicles (UAV) technology, and the increased demand for such vehicles, launched either from another air vehicle or from the ground, have led to the development of UAVs that can be launched initially with folded wings and unfolded subsequently in free flight. During the morphing stage, rapid changes in the aerodynamics raise concerns about the aircraft's structural stability, especially during the deployment of folded wings [3]. Behrbohm [4] discovered the advantages of the close-coupled canard/wing configuration in airplane design. However, progressively lighter and more powerful aircraft engines and higher flight speeds obviated the need for the additional wing. Recent studies have shown, however, that closely coupled dual-wing systems possess aerodynamic advantages over the single-wing configuration in terms of both fuel efficiency and lower drag [5–7].

Er-El and Seginer [8] carried out experiments on close-coupled wing-canard and wing-alone configurations, and studied the effects of the canard sweep angle and the longitudinal position of the shedded leading-edge vortex (LEV) by the canard and wing. Results showed that the canard had actually displaced the LEV of the wing upward and outboard in the wake. The angle of attack at which the LEV would break down for the wing-canard configuration was 8–10 deg higher than that for the wing-alone configuration. Nenadovitch [9] discovered the improved lift aerodynamics while conducting two-dimensional tests for dual-wing configurations and the equivalent single-wing configurations. Olson and Selberg [10] compared dual wings and single wings of the same lift capacity in experiments with three-dimensional models. Their findings also showed that dual-wing configurations could achieve substantially higher lift-to-drag ratios than a single wing at regions below the maximum lift coefficient ($C_{L,\max}$). Wolkovitch [11] conducted wind tunnel tests so as to verify the Prandtl–Munk theory, which predicts that tandem-wing configurations with a large (vertical) gap would have substantially lower induced drag than conventional wing-tail configurations of similar span. The results confirmed further the prediction by the Prandtl–Munk theory.

Many of the current numerical and experimental investigations involving these multi-surface configurations have been conducted at Reynolds numbers above 10^6 . This is primarily due to the fact that this is where conventional aircrafts currently operate. The

experiments conducted by Feistel et al. [12] were at a Reynolds number of $1.4 \cdot 10^6$ for a set of finite-span wings. The results showed that some configurations were favorable for the presence of a canard (increased $C_{L\max}$), decreasing in the maximum lift coefficient of the wing. Rhodes and Selberg [13] investigated the aerodynamics of a closely coupled dual-wing aircraft with the swept-forward and swept-rearward wing arrangement. The results were compared with those of a corresponding single-wing aircraft and showed that the lower drag of the dual-wing configurations was due to the combination of two- and three-dimensional drag reduction. The structural advantages of the two wings, which permitted higher aspect ratios for the two-wing systems, were due largely to the wing-tip structural connection.

In our present research, we focus on lower Reynolds numbers ($Re < 10^6$). It is well known that the aerodynamics at low Reynolds numbers should be more complex because the boundary layers would become less capable of handling adverse pressure gradients. Laminar or turbulent separation bubbles are common, and unless they are properly controlled, they may lead to excessive drag and lower lift [14]. Scharpf and Muellert [15] conducted a wind-tunnel test for the tandem-wing models with two identical 6-in.-chord Wortmann FX63-137 airfoils in closely coupled tandem configurations at a Reynolds number of $8.5 \cdot 10^4$. Flow visualization using kerosene smoke was performed to complement the experiment. The results showed that the total drag reduction and lift increase resulted in a significant increase in the lift-to-drag ratio for a number of tandem-wing configurations.

Because of the recent interest in the viability of the tandem-wing aircraft, in the present research, we chose a generic tandem-wing UAV model as the research object. The impact of the aerodynamic effects on the lift and drag characteristics of the tandem wing caused by the dynamic deflection during the entire morphing stage between the canard and wing will be analyzed. The corresponding moments experienced by the hinges during the morphing stage will also be investigated.

II. Flow Configuration and Computational Fluid Dynamics Method

A. Flow Configuration

As shown in Fig. 1, the three main factors affecting the performance of a closely coupled dual-wing system with the same airfoil shape and equal chords are stagger, St , which is the longitudinal separation of the wings; the gap, G , which is the vertical distance between the wings; and decalage, δ_c (δ_w), which is the angle of the canard and wing with respect to the x and y axes [13]. Both St and G are measured from midchord to midchord and are nondimensionalized with respect to the chord length, c .

The length of the UAV model fuselage, L , is 0.6 m, and the radius, R , of the frontal cross fuselage is 0.047 m. The JED-EJ75 airfoil is used as the UAV canard and wing. Because of its high curvature, the airfoil can be folded easily and attached tightly to the UAV fuselage. The main geometric characteristics of the canard and wing are a constant chord, c , of 0.0647 m across the span, a reference wing area, S , of 0.0663 m², a wing span, b , of 1.025 m, and a wing aspect ratio, AR , of 15.84. From c and S , one can calculate the wing span, b , and the wing aspect ratio, A .

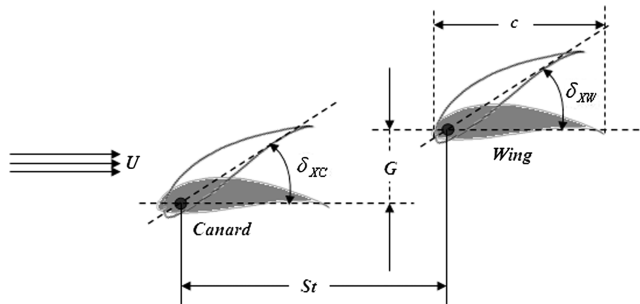


Fig. 1 The parameter definition of the canard and wing.

As shown in Figs. 2a–2c, the first morphing stage is defined as that in which the canard and the wing are being unfolded (Figs. 2a and 2b), while the second morphing stage is defined as that after the unfolding of the canard and wing. They then rotate (either clockwise or counterclockwise) to their final orientation with respect to the x -axis (Fig. 2c).

The morphing angles of the wing and canard in the first morphing stage are $\delta_{yw} = 0 \sim 90$ deg, $\delta_{yc} = 0 \sim 90$ deg and in the second morphing stage they are $\delta_{xw} = 0 \sim 39.3$ deg, $\delta_{xc} = 0 \sim 141$ deg. Both St and G can strongly affect the aerodynamics of the tandem UAV. If St is very small, the interaction between the canard and wing will become stronger. On the other hand, if St is very large, the aerodynamic coupling effects between the canard and wing cannot be used effectively. In addition, for the folded structure consideration, St must be large enough to fit the entire wing span. To reduce the downwash effect caused by the canard, an upper-wing layout (the wing is located above the canard) was chosen. The advantage of having a lower canard and an upper-wing configuration is to avoid the structural conflict between the folded components during the morphing stage. Hence, St is chosen as $3c$ and G is $1.2c$. Table 1 summarizes the UAV model geometry and flight conditions.

B. Computational Fluid Dynamics Method

1. Dynamic Grid Technology

The simulation was conducted using computational fluid dynamics (CFD) and ANSYS/FLUENT V.6.3.26, in which a dynamic grid technology was used to simulate the unsteady flowfield boundary movement. On one hand, the boundary movement (speed or angular velocity) can be predefined and specified before the calculation. On the other hand, the boundary movement cannot be predefined, but it can be determined from the previously calculated results. The grid updating stage would be changed automatically by the program according to each iteration step.

The dynamic grid has three common methods: dynamic layering, spring-based smoothing, and local remeshing. In the present situation, we adopt the last two methods.

The integral form for any flow scalar, Φ , in any control body's transport equation can be written as

$$\frac{d}{dt} \int_V \rho \phi dV + \int_{\partial V} \rho \phi (\vec{u} - \vec{u}_g) \cdot d\vec{A} = \int_{\partial V} \Gamma \nabla \phi \cdot d\vec{A} + \int_V S_\phi dV \quad (1)$$

where ρ is gas density, \vec{u} is uniform flow velocity, \vec{u}_g is moving mesh speed Γ is dissipation factor, S_ϕ is the source term, and dV stands for control volume boundary.

The fundamental difference between the moving-mesh transport equation and an ordinary transport equation lies in the representative grid movement:

$$-\int_{\partial V} \rho \phi \vec{u}_g \cdot d\vec{A} \quad (2)$$

The first-order backward difference discrete is

$$\frac{d}{dt} \int_V \rho \phi dV = \frac{(\rho \phi dV)^{n+1} - (\rho \phi dV)^n}{\Delta t} \quad (3)$$

where n and $n+1$ represent the current time and the subsequent moment, respectively. The control volume V^{n+1} at any $n+1$ moment can be calculated as

$$V^{n+1} = V^n + \frac{dV}{dt} \Delta t \quad (4)$$

where $\frac{dV}{dt}$ is the derivative of the control volume with respect to time, which could be defined as

$$\frac{dV}{dt} = \int_{\partial V} \vec{u}_g \cdot d\vec{A} = \sum_j^{n_f} \vec{u}_{g,j} \cdot \vec{A}_j \quad (5)$$

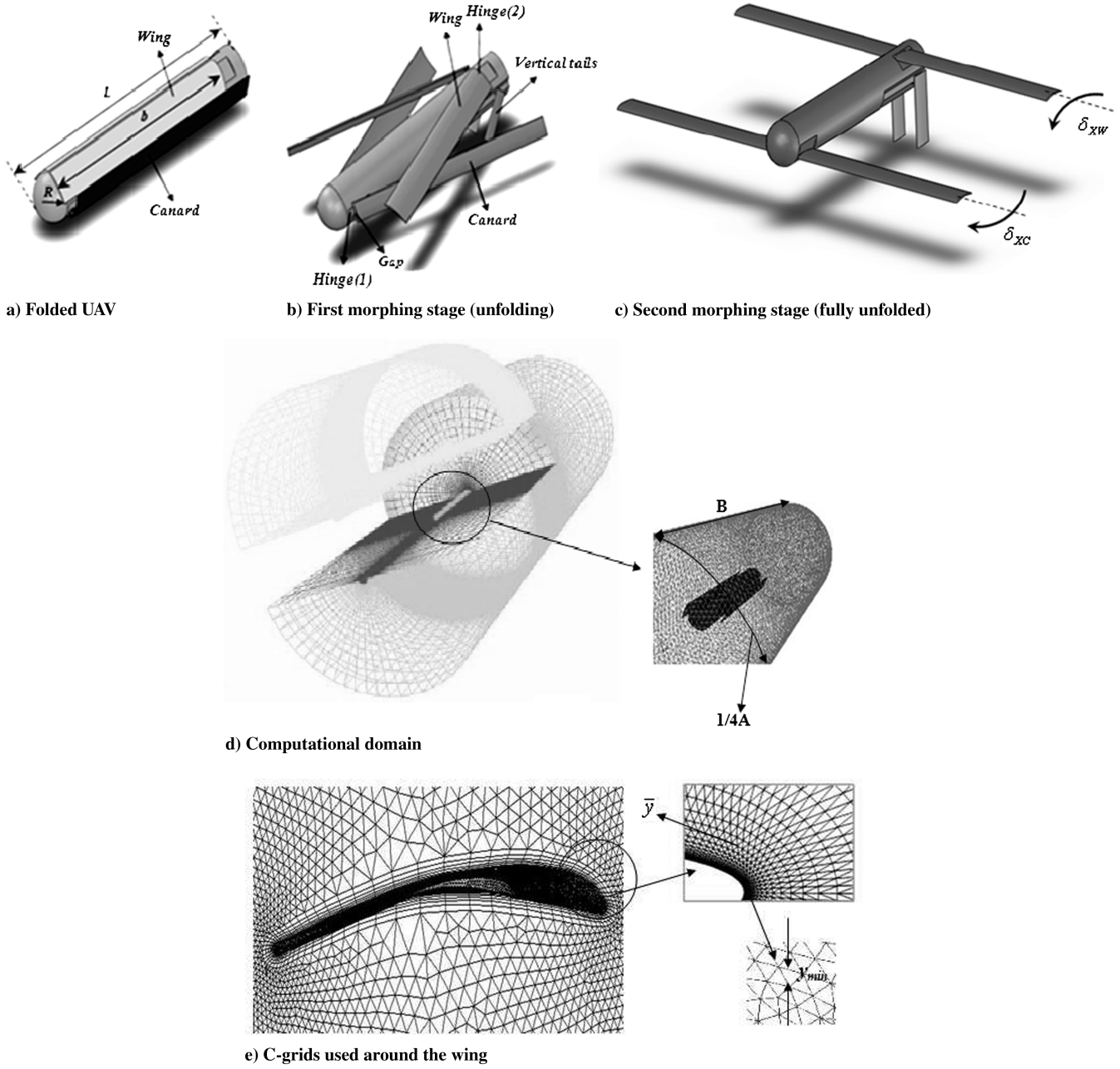


Fig. 2 Illustration of morphing stages.

where n_f represents the number of control volume boundary. Equation (5) can be written as

$$\sum_j^{n_f} \vec{u}_{g,j} \cdot \vec{A}_j = \frac{\delta V_j}{\Delta t} \quad (6)$$

where δV_j is the swept volume of control body's j -surface within Δt time.

2. Boundary Conditions

The wing and canard will produce unsteady aerodynamic force during the morphing stage. Nonstructural dynamic grids have been employed. The folding components at the hinge, such as the torsion spring, etc., were removed to improve simulation efficiency.

When modeling the whole aircraft, the results will be significantly affected by the quality of the mesh. As shown in Figs. 2d and 2e around the wing and the canard, a size function control is adopted to improve the mesh density. The radial length of the computational

Table 1 Summary of UAV geometry and flight conditions

Geometric parameters	Wing and canard
Reference wing area S , m^2	0.0663
Wing span b , m	1.025
Wing chord c , m	0.0647
Aspect ratio, b/c	15.84
Fuselage L , m	0.6
Radius of head R , m	0.047
Morphing angles, deg	$\delta_{YW} = 0 \sim 90$ deg, $\delta_{YC} = 0 \sim 90$ deg (first morphing stage) $\delta_{XW} = 0 \sim 39.3$ deg $\delta_{XC} = 0 \sim 141$ deg (second morphing stage)
Re	1.3×10^5
St	3c
G	1.2c
Freestream velocity U , m/s	30

domain is 30 times the cross section of the fuselage. The computational domain is divided into 24 subregions, with fine grids concentrating on the regions close to the body surface.

The finest grid has minimum spacing at the wall of $y = 3.0e^{-5c}$, where c is the chord length of the wing. The average \bar{y} near the wall surface is between 10-to-1 or 20-to-1 of y . The turbulent boundary layer with the first grid point from the wall at y^+ is approximately 30. Thus, a wall function has been used in the computation. The entire grid is smoothed and swapped to improve the accuracy of the calculation.

The lift, drag, and hinge moments are evaluated at freestream $U = 30$ m/s, corresponding to a Reynolds number, Re , of $1.6 \cdot 10^5$ based on the wing-mean aerodynamic chord, c . Implicit formulations are used in the boundary conditions.

III. Results and Discussion

A. Comparison of the Simulation and Experimental Results

We first tested the grid sensitivity and the results are shown in Fig. 3. We chose six different grid sizes ($A \times B, y$) to simulate the whole morphing motion of the tandem aircraft. A represents the nodes on the perimeter edges of the outer computational domain; B represents the nodes in the axial direction; y represents the minimum grid spacing at the wall; and c is the chord length of the wing. The grid sizes ($A \times B, y$) are $201 \times 201, 3e^{-5c}$; $401 \times 201, 3e^{-5c}$; $201 \times 101, 2e^{-5c}$; $201 \times 101, 5e^{-5c}$; $201 \times 101, 0.5e^{-5c}$, and $201 \times 101, 3e^{-5c}$. From Fig. 3, we can see the six grid sizes studied do not deviate from each other within 1%. As a result, we adopted the $401 \times 201, 3e^{-5c}$ grid for the subsequent computation.

The reliability of the numerical method must be verified. The geometric parameters of the model were the same as those used in the wind-tunnel test performed by Scharpf and Muellert [15]. Both the wing and the canard were FX63-137 airfoils with chord lengths of 6 in. and aspect ratios of 2.67. The lift and drag characteristics of the tandem case at different angles for the canard and wing δ (δ_{XC}, δ_{XW}) are compared.

As shown in Fig. 4a the numerical results are in excellent agreement with the wind-tunnel experimental data. As expected, the single airfoil is seen to stall at about $\delta_{XW} = 16$ deg. After introducing the canard into the flow, the lift coefficient of the wing became lower than that of the single airfoil baseline case at almost all angles of attack. This is in part due to the decrease in the effective angle of attack because of the strong downwash effect caused by the canard. On the other hand, it may also be due to the fact that the downwash vortex shed by the canard has generated a low-pressure region below the wing, which would have contributed to the loss of lift experienced by the wing. Both effects cause the lift curves of the wing ($\delta_{XC} = 0$ deg, $\delta_{XC} = 10$ deg) to gradually become flat at higher δ_{XW} , and the curve for $\delta_{XC} = 0$ deg is always above the

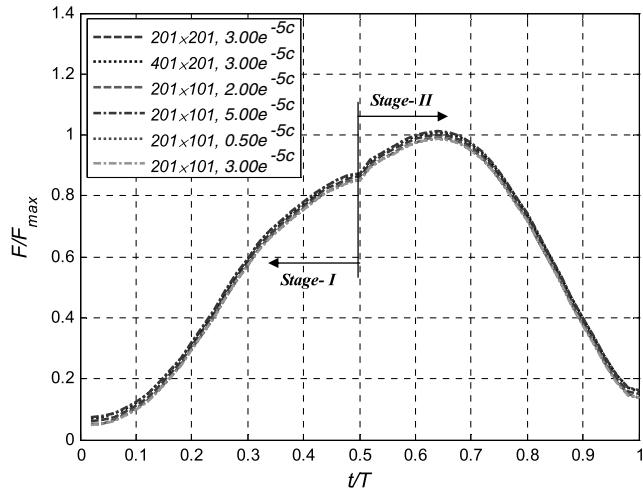
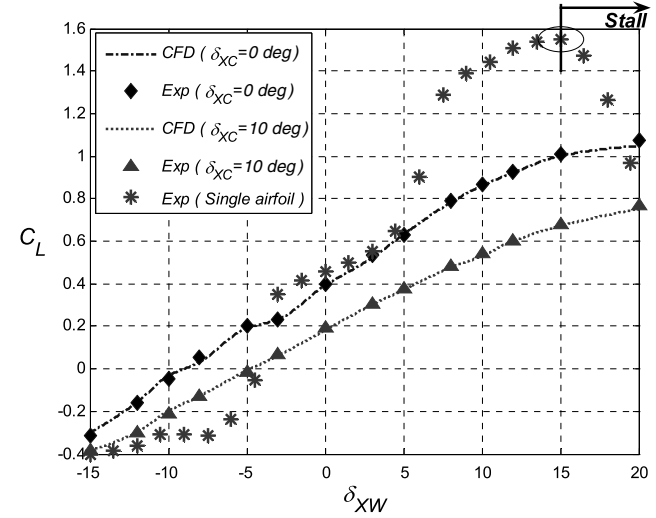


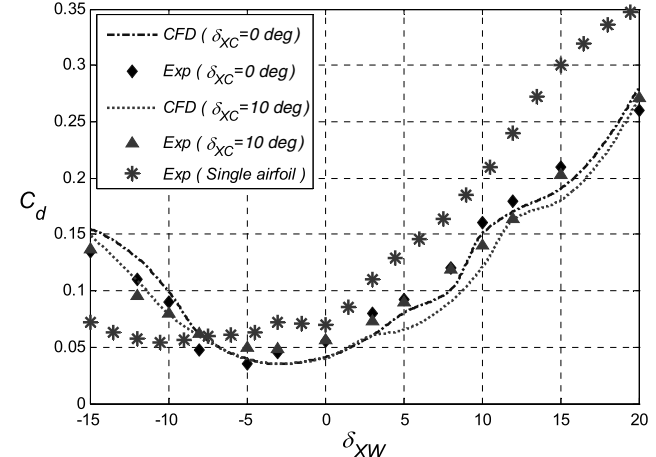
Fig. 3 Grid sensitivity test.

curve for $\delta_{XC} = 10$ deg. Both curves have indicated a delay in the onset of stall ($\delta_{XW} = 16$ deg) compared with the single airfoil case.

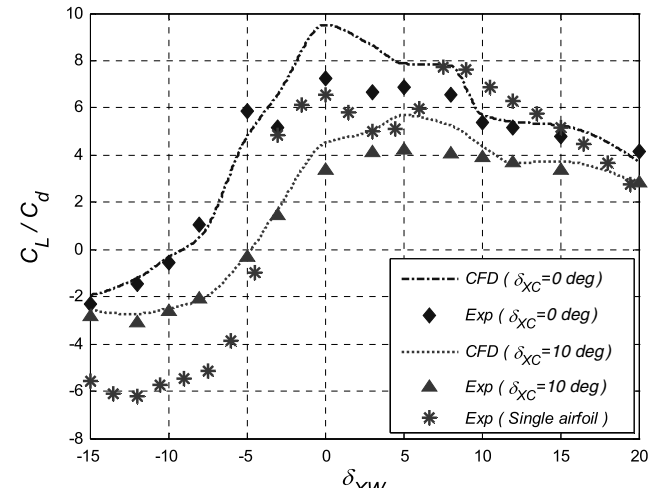
The drag coefficients of the tandem wing were obviously lower than those of the single wing when $\delta_{XW} > -8$ deg, especially when δ_{XW} reached 20 deg. The drag of the wing was reduced by a maximum of 24%. This can be mainly attributed to the fact that the wing is subjected to the downwash flow induced by the canard. The



a) Lift coefficient



b) Drag coefficient



c) Lift-to-drag ratio

Fig. 4 Variation of lift and drag characteristics for the tandem wing. (Experimental data are taken from Scharpf and Muellert [15].)

downwash flow could weaken the momentum of the flow impinging on the wing and, as a consequence, the resistance of the wing would be reduced. Figure 4c shows the simulated lift-to-drag ratio comparing with experimental data. The maximum is always at about $\delta_{XW} = 0$, as may have been expected from the C_L and C_d presented earlier.

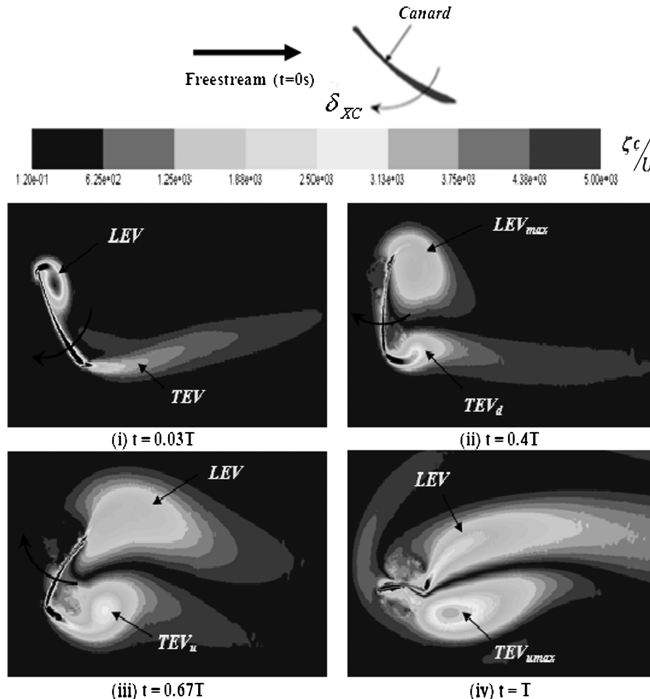
After the reliability of the numerical method was verified, the simulation of the whole morphing UAV commenced. To study the effect of vortex interferences, we shall focus first on the second

morphing stage. That is, after the canard and wing are fully unfolded and are rotating toward their final orientations.

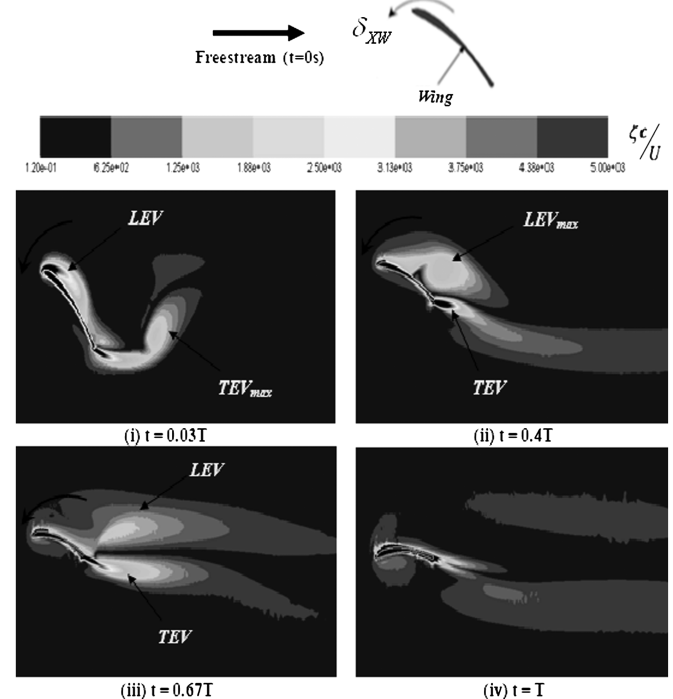
B. Vortex Interaction

1. Single Canard

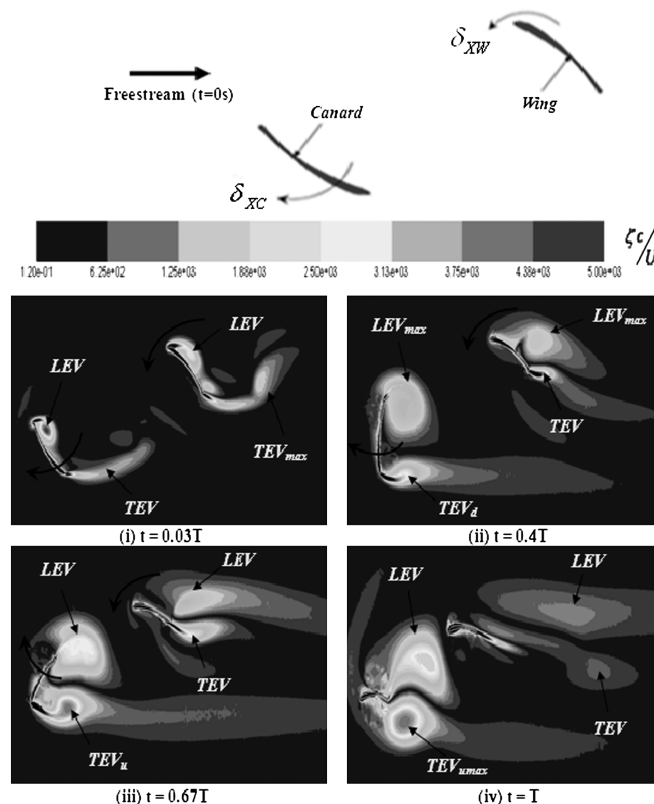
As shown in Fig. 5a at $t = 0.03T$, the leading edge of the canard during the downstroke stage generated the LEV, and at the trailing edge a long “tail” is also generated (trailing-edge vortex, TEV) but



a) Single canard



b) Single wing



c) Tandem wing

Fig. 5 Contours of normalized vorticity magnitude $\xi c/U$ at different times and at zero AOA.

the strength is relatively weak. At $t = 0.4T$ (transition position), the upstroke starts. The LEV has become stronger and reaches its maximum (LEV_{\max}). The TEV_d has also grown stronger during this period. After the transition position, at $t = 0.67T$, the LEV starts to weaken. However, the TEV_u continues to grow stronger due to the upstroke motion. By this time, the TEV_u occupies almost 50% of the chord length of the canard's lower surface. When the canard completes its upstroke motion and becomes parallel to the main flow ($t = T$), the LEV gradually breaks down while the TEV reaches its maximum strength ($\text{TEV}_{u\max}$).

2. Single Wing

From Fig. 5b, we can see that the single wing has also created its own LEV and TEV at the beginning of the morphing stage. Before $t = 0.4T$, the strength of the LEV is still growing but it has already created an obvious vortex center. On the other hand, the TEV always appears to be unstable during the whole morphing stage and breaks down earlier than the LEV (i.e., after $t = 0.67T$). Because the single wing has a smaller deflection angle than the canard and without the downwash effect created by the front canard, both the LEV and TEV formed would break down earlier than is the case with the single canard.

3. Tandem Wing

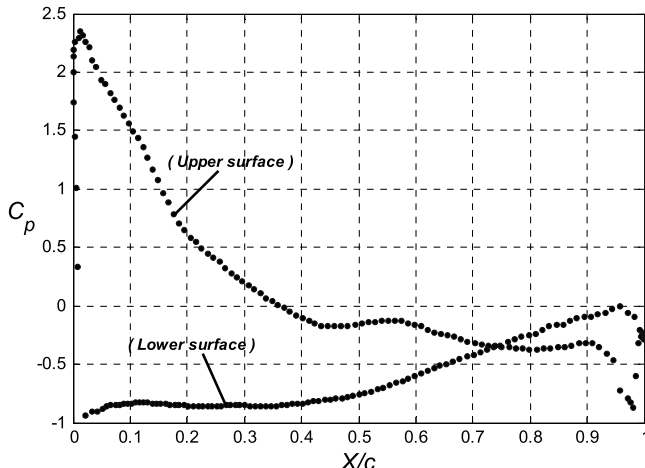
As shown in Fig. 5c, normalized vorticity contours are presented for the tandem wing at different times and at a constant angle of attack of zero degrees. Lift and drag coefficients will be presented to give the combined effect of the tandem airfoils. The results will also be

compared to the baseline case consisting of a single airfoil under the same flight conditions as the tandem-airfoil arrangement.

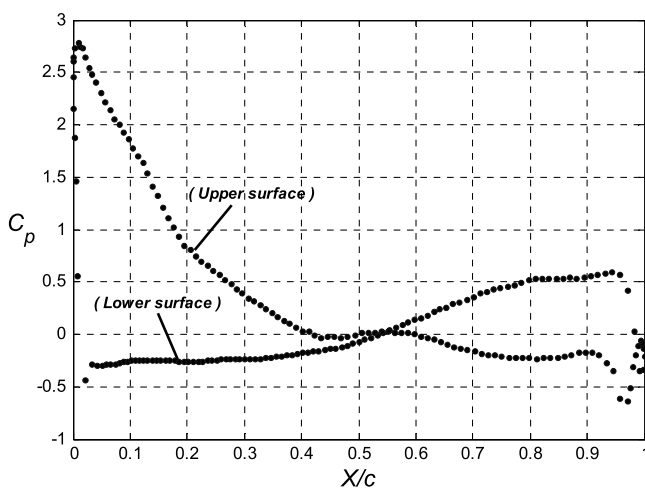
At $t = 0.03T$, both the canard and wing have created their own LEV and TEV, but the vortex strength is relatively weaker than those of the corresponding single canard and single wing cases. It is obvious that St and G can effectively control the aerodynamics between the canard and the wing. At an early time ($t = 0.03T$), the aerodynamics of the canard and wing are mainly determined by their own vortex strengths. By $t = 0.4T$ (transition position), the LEV of the canard and wing have both reached their maximum. Because of their relatively close position to each other, the downwash and upwash effects dominate in this period. By $t = 0.67T$, due to the strong upwash effects from the rear wing, it can effectively control the incident flow of the front canard, so that the LEV of the tandem-wing canard is more concentrated than that of the single canard. The vorticity contour field is also smaller in size and forms a stable vortical structure. This in turn can enhance the vortical lift force of the canard. For the rear wing, the front canard would induce a strong downwash effect. Because the rear wing is always under the influence of the downwash airflow, the LEV of the tandem-wing case shows relatively weaker strength than the single-wing case. Compared to the single wing, the LEV_{\max} of the tandem wing is also not highly concentrated and breaks down earlier. This in turn affects the lift of the wing, which decreases by the end of the morphing stage.

C. Pressure Coefficient

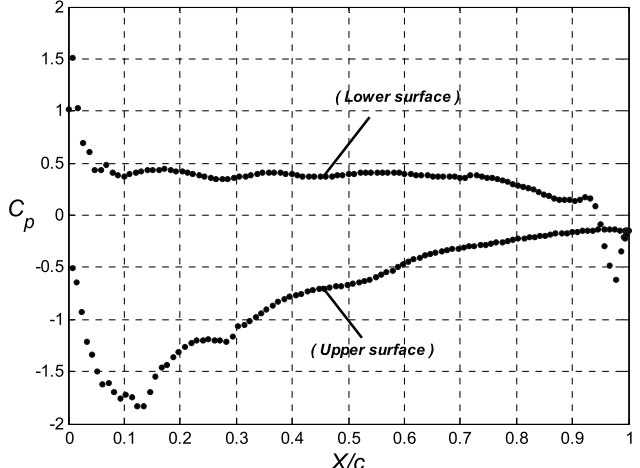
The pressure coefficient is negative for pressure less than the freestream, which may occur on the top or bottom surface of the wing



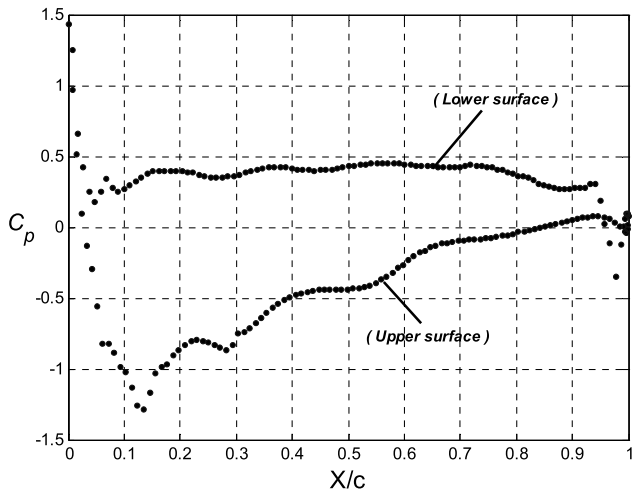
a) Single canard



b) Tandem canard



c) Single wing



d) Tandem wing

Fig. 6 Pressure coefficient (C_p) at $t/T = 0.67$.

or canard. The data from the simulation are expressed with respect to the local chord length c . Figure 6 shows the pressure coefficient (C_p) distribution on the single wing, the single canard, and the tandem cases at $t = 0.67T$.

Before the canard starts the upstroke motion, the upper surface of the canard is actually playing the role of “the lower surface.” Contrary to the conventional airfoil theory, the higher pressure region is on the top surface of the canard (upper surface), and the lower pressure region is on the bottom of the canard (lower surface). After the upstroke starts, both the upper and lower surfaces have reversed.

As for the wing shown in Figs. 6c and 6d, the pressure distribution resembles the conventional airfoil theory. However, the pressure coefficient difference between the upper and lower surfaces in the tandem case is relatively smaller than that of the single-wing case due to the earlier breakdown of the LEV and the influence of the TEV from the front canard.

D. Lift and Drag Characteristics

From Fig. 7a, the lift characteristics for the canard and wing in the tandem case have been changed to a certain extent. The maximum difference of C_L for the canard and wing in the tandem case is 0.5 and 0.25, respectively ($t = 0.43 \sim 0.87T$). This shows clearly that the aerodynamic interference and mutual coupling between the canard and the wing have created effects on the lift characteristics of the whole UAV during the second morphing stage.

The significant rise in lift seen under these conditions for the canard is the direct result of the increase in the pressure difference across the top and bottom surfaces of the rear wing in the tandem case. Between $t = 0.43T \sim 0.87T$, C_p distributions on the upper surface of the canard do not change significantly; the lower surface of canard, however, experiences an increase in pressure (see Figs. 5a and 5b). Meanwhile, due to the upwash effect created by the rear wing, the effective angle of attack to the canard increases. These two factors contribute to the increase in lift for the canard in the tandem case (see Fig. 7a). After $t > 0.87T$, the vortex strength of the wing gradually weakens and breaks down eventually. The canard would then have relatively smaller upwash effects created by the rear wing. After this transition position, the lift curves for the single and tandem case become almost identical.

Between $t = 0.43T \sim 0.87T$, due to the downwash effect created by the front canard, the effective angle of attack to the rear wing would be reduced, and so the lift curve of the wing in the tandem case is always below that of the single wing during the second morphing stage. After $t = 0.87T$, the LEV generated by the front canard has become stronger, which would easily control the incident flow of the rear wing and the downwash effect remains. As a result, the lift curve of the wing in the tandem case is still below that of the single wing.

In contrast, the drag characteristics do not show clear changes except for small changes during a short period ($t = 0.43T \sim 0.87T$). The vortex generated by the rear wing is obviously much weaker than that of the canard and breaks down earlier. This, however, will have no effect on the formation of drag of the front canard and so the curve remains the same as that of the single canard.

The wing will not experience transition deflection during the second morphing stage except for some slight difference made by the downwash effect from the front canard. Hence, the drag coefficients for the rear wings are almost identical to that of the single wing after $t = 0.87T$.

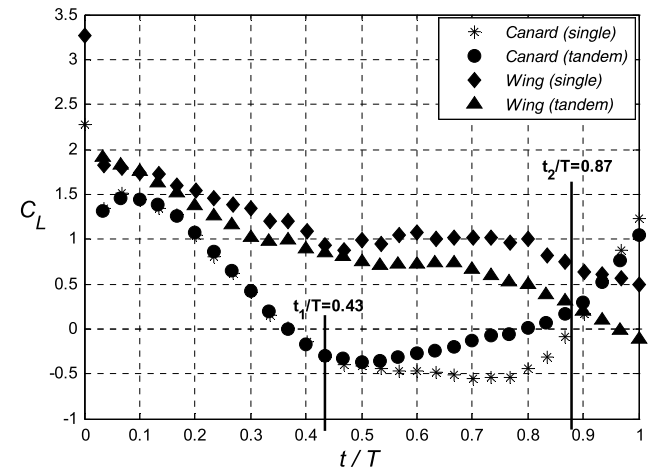
As shown in Fig. 7a, before the canard and wing complete their second morphing motion, the lift coefficients (C_L) show a nonlinear decay. It is well known that the lift coefficient of the wing (no deflection) in steady flow with angle of attack (AOA) = 0 deg should always tend to be near the zero level if the wing is symmetrical or to very small values if the wing is cambered. However, due to the dynamic deflection, the lift coefficients could fluctuate ($C_L = -0.5 \sim 2$), while the drag coefficients can become almost 14 times larger than that of the final steady condition (fully unfolded) at $t = 0.26T$ (Fig. 7b). This suggests that the dynamic deflection strongly affects the lift and drag characteristics of the tandem UAV. During the morphing stage, if the UAV designer does not account for these changes smoothly, they could affect the success of the morphing motion.

E. Hinge Moment and Damping During the Whole Morphing Stage

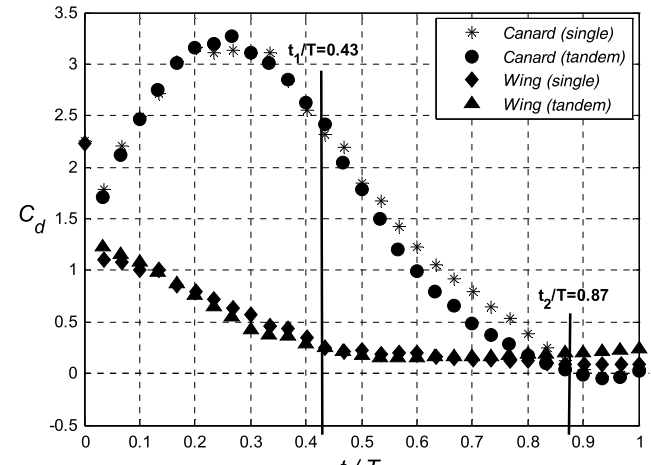
From Fig. 8, we can see that both the folding wing and the canard have generated their own hinge moments around the rotation axis. As shown in Fig. 8a, during the first morphing stage, both the wing and the canard rotate 90 deg ($\delta_{YW} = 0 \sim 90$ deg, $\delta_{YC} = 0 \sim 90$ deg). Because of their initial positions, the projection areas perpendicular to the flow direction increase rapidly during the morphing stage. The corresponding hinge moment increases continually and finally reaches a maximum at $\delta_{YC} = 90$ deg. A significant increase in the hinge moment is also observed during the first morphing stage, but the sign of the moment remains the same throughout.

We should not ignore the aerodynamic interference between the canard and the rear wing in the tandem case during the first morphing stage. As discussed in Sec. III.B, the canard has a downwash effect on the rear wing. These considerable effects would also be manifested in the hinge-moment characteristics. With these effects in mind, we can clearly see that, different from the canard, the hinge moment of the rear wing shows obvious nonlinear characteristics and it reaches a maximum at $\delta_{YW} = 60$ deg.

Compared with the first morphing stage, during the second morphing stage, as shown in Figs. 8b and 8c, both the canard and the wing have to rotate to their final orientations, $\delta_{YW} = 0 \sim 39.3$ deg and $\delta_{YC} = 0 \sim 141$ deg. However, due to the large deflection angles (especially for the canard, where $\delta_{YC} = 90$ deg is the transition deflection angle), the hinge moment changes to the opposite direction. These changes include the rapid change in the sign for the



a) Lift coefficients (C_L) for the single canard/wing vs tandem canard/wing



b) Drag coefficients (C_d) for the single canard/wing vs tandem canard/wing

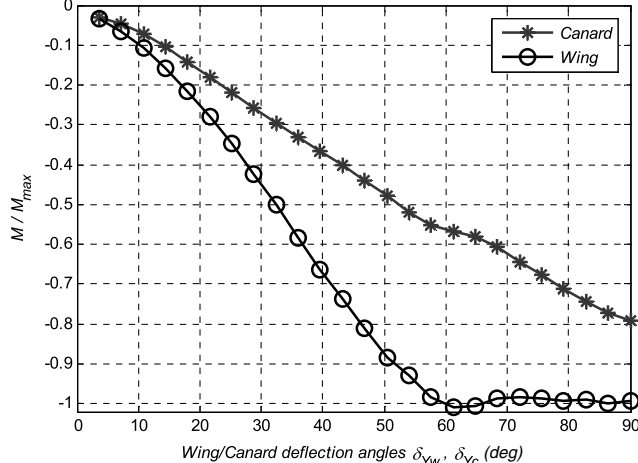
Fig. 7 The lift (C_L) and drag (C_d) coefficients during the second morphing stage.

hinge moment and a difference is the corresponding magnitude, by (+)57% and (+)260% for the canard and wing, respectively.

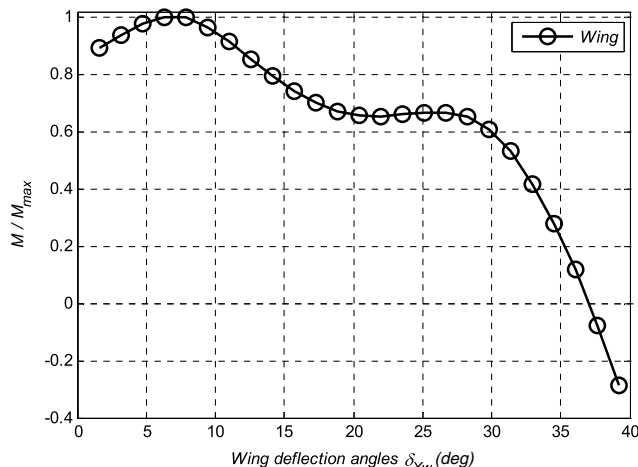
As shown in Fig. 9, the damping that the wing and canard in the tandem case need to endure is obviously different during the morphing stage. The damping of the rear wing is obviously larger than that of the front canard, by about 1.2 times. This is mainly due to the lower front canard aerodynamic layout. Because the canard is located below the wing, it could create downwash airflow to the rear wing. Coupled with the impact of the air flow, the wing surface would

carry more damping. However, for the second morphing stage, the wing deflection is less than 40 deg, and its projected area perpendicular to the flow direction decreases rapidly in the first morphing stage. Therefore, the corresponding damping decreases nonlinearly. As shown in Fig. 9c, due to the fact that the canard would experience deflection from 5.63 to 141 deg, there is a transition condition. Therefore, the canard initially experiences an increasing and then a decreasing trend during the morphing stage.

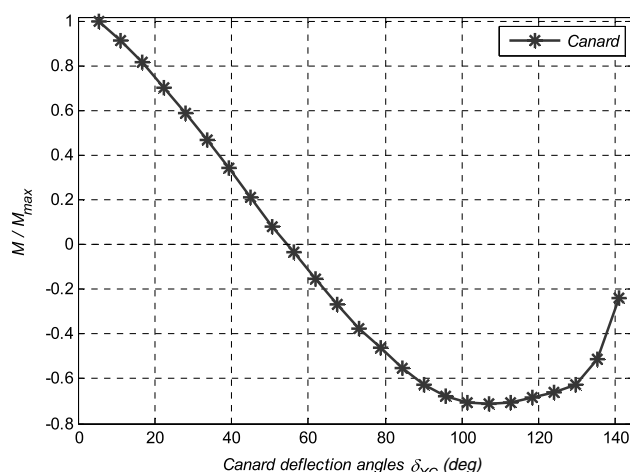
Finally, the hinge moment and the center of pressure position of wing and canard in the tandem case are plotted against the wing-tip



a) Canard and wing in tandem case during the first morphing stage

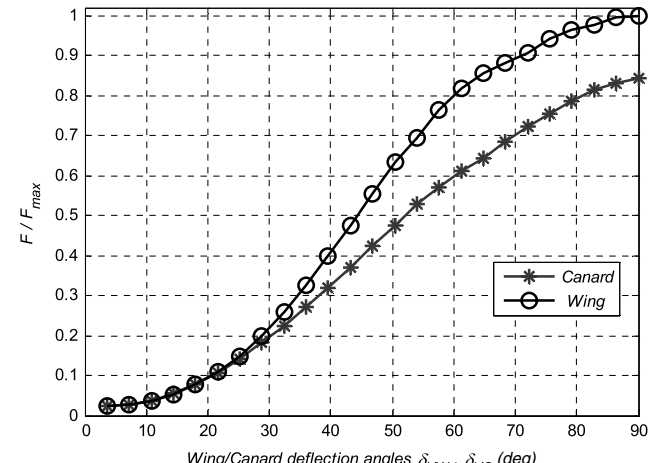


b) Wing in tandem case during the second morphing stage

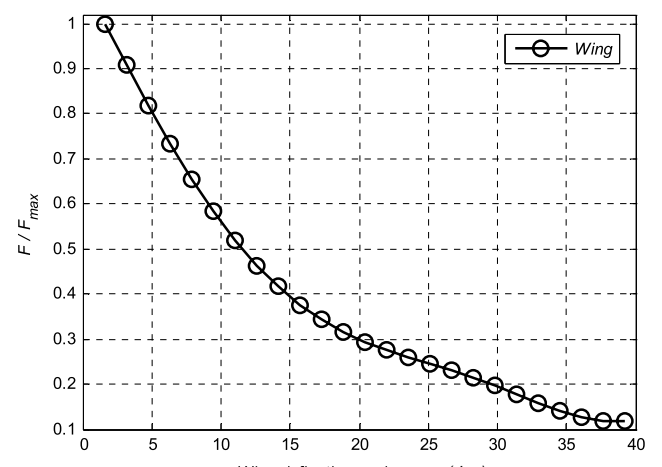


c) Canard in tandem case during the second morphing stage

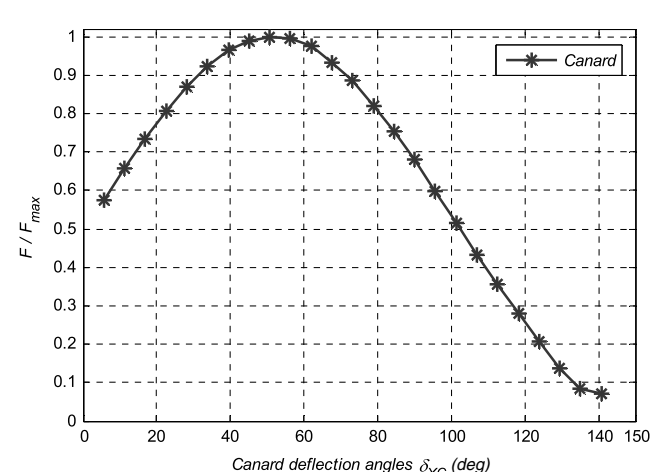
Fig. 8 The hinge moment during the whole morphing stage.



a) Canard and wing in tandem case during the first morphing stage

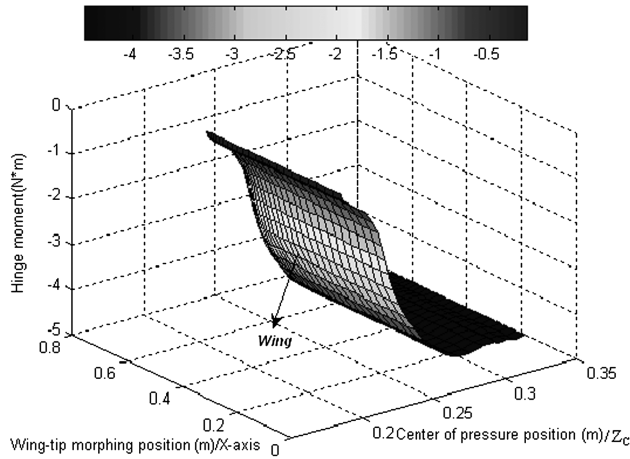


b) Wing in tandem case during the second morphing stage

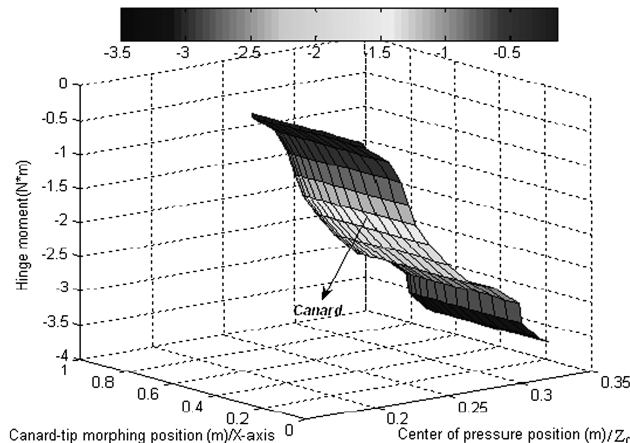


c) Canard in tandem case during the second morphing stage

Fig. 9 The damping during the whole morphing stage.



a) The wing-tip morphing position



b) The canard-tip morphing position

Fig. 10 The hinge moment and the center of pressure position.

morphing position in Fig. 10a and against the canard-tip morphing position in Fig. 10b. The influences on the dynamic response by the aircraft's center of pressure shift are shown in these two figures. Different from the dynamic equations for the fixed-wing configuration, the tandem-wing aircraft is a multibody dynamic system during the morphing stage because the morphing motion causes the whole tandem aircraft's center of pressure position to shift backward. This will create some effects on the moment by gravity relating to the origin that is fixed on the fuselage of aircraft when the pitch angle is not zero, which consequently affects the dynamic response. Although the shift of the center of pressure is small, the effects on the moment created by the backward movement of the center of pressure position could be large enough to cause certain effects on the dynamic response.

IV. Conclusions

Based on the results of our study, the following conclusions can be drawn:

1) Compared with the single wing and the single canard during the second morphing stage, the aerodynamic characteristics of the canard and wing in the tandem case have been modified. Between $t = 0.43T$ and $0.87T$, the canard vortices and wing vortices generated in the tandem case can mutually affect the aerodynamics of the other, causing an increase in lift coefficient for the canard and a decrease in lift coefficient for the wing. However, they do not seem to have an effect on the corresponding drag characteristics.

2) Contrary to the conventional airfoil theory, during the beginning of second morphing stage, both the upper and lower surfaces have reversed. After the upstroke motion starts, the pressure coefficient distribution on the single canard shows better agreement with the

conventional theory. Moreover, in a tandem canard and wing layout, the onset of turbulent transition seems to appear earlier (by 13% of the chord length) on the canard upper surface.

3) During the first morphing stage, both the folding wing and the canard create their own hinge moments around their respective rotational axes. The hinge moment increases continuously during the entire unfolding stage. The unsteady aerodynamics has larger effects during the second morphing stage. Because of the transition deflection angle and at a certain point in time, the hinge moment changes to the opposite direction. The magnitude also differs, by (+) 57% and (+) 260% for the canard and wing, respectively.

4) The damping generated by the wing and canard also shows obvious differences during the whole morphing stage. During the first morphing stage, the damping of the wing is larger than that of the canard, by about 1.2 times. In the second morphing stage, due to the wing deflection of less than 40 deg, the corresponding damping decreases more gradually than the canard.

References

- [1] Wlezien, R., Horner, G., McGowan, A., Padula, A., Scott, M., Silcox, R., and Simpson, J., "The Aircraft Morphing Program," NASA TM-1998-208150, 1998; also AIAA Paper 98-1927.
- [2] Niksch, A., Valasek, J., and Stroganac, T., "Morphing Aircraft Dynamical Model: Longitudinal Shape Changes," AIAA Paper 2008-6567, Aug. 2008.
- [3] Evgeny, S., Moti, K., and Yuval, L. "Generalized Approach to Aeroelastic CFD Time Simulations of Morphing Flight Vehicles," AIAA Paper 2009-2323, May 2009.
- [4] Behrbohm, H., "Basic Low-Speed Aerodynamic of Short-Coupled Canard Configuration of Small Aspect Ratio," SAAB TN-60, Linkoping, Sweden, 1965.
- [5] Rival, D., Schoenweitz, D., and Tropea, C., "Vortex Interaction of Tandem Pitching and Plunging Plates: A Two-Dimensional Model of Hovering Dragonfly-Like Flight," *Bioinspiration & Biomimetics*, Vol. 6, No. 1, 2011, pp. 1–13.
doi:10.1088/1748-3182/6/1/016008
- [6] Rival, D., Hass, G., and Tropea, C., "Recovery of Energy from Leading- and Trailing-Edge Vortices in Tandem-Airfoil Configurations," *Journal of Aircraft*, Vol. 48, No. 1, 2011, pp. 203–211.
doi:10.2514/1.C031062
- [7] Lim, K. B., and Tay, W. B., "Numerical Analysis of the s1020 Airfoils in Tandem Under Different Flapping Configurations," *Acta Mechanica Sinica (English Edition)*, Vol. 26, No. 2, 2010, pp. 191–207.
doi:10.1007/s10409-009-0302-2
- [8] Er-El, J., and Seginer, A., "Vortex Trajectories and Break Down on Wing-Canard Configurations," *Journal of Aircraft*, Vol. 22, No. 8, 1985, pp. 641–648.
doi:10.2514/3.45180
- [9] Nenadovitch, M., "Aerodynamics—The Characteristics of Certain Rigid Biplane Frames with an Infinite Wingspan," *Comptes Rendus Hebdomadaires des Séances de l'Academie des Sciences*, Vol. 201, 1935, pp. 385–386.
- [10] Olson, E. C., and Selberg, B. P., "Experimental Determination of Improved Aerodynamic Characteristics Utilizing Biplane Wing Configurations," *Journal of Aircraft*, Vol. 13, No. 4, 1976, pp. 256–261.
doi:10.2514/3.44523
- [11] Volkovitch, J., "Subsonic VSTOL Aircraft Configurations with Tandem Wings," *Journal of Aircraft*, Vol. 16, No. 9, 1979, pp. 605–611.
doi:10.2514/3.58574
- [12] Feistal, T. W., Corsiglia, V. R., and Levin, D. B., "Wind Tunnel Measurements of Wing-Canard Interference and a Comparison with Various Theories," *Society of Automotive Engineers*, Vol. 90, No. 2, SAE Technical Paper 810575, Troy, MI, 1981, pp. 2026–2039.
- [13] Rhodes, M. D., and Selberg, B. P., "Benefits of Dual Wings over Single Wings for High-Performance Business Airplanes," *Journal of Aircraft*, Vol. 21, No. 2, 1984, pp. 116–127.
doi:10.2514/3.48234
- [14] Carmichael, B. H., "Low Reynolds Number Airfoil Survey," NASA CR-165803, 1981.
- [15] Sharpf, D. F., and Muellert, T. J., "Experimental Study of a Low Reynolds Number Tandem Airfoil Configuration," *Journal of Aircraft*, Vol. 29, No. 2, 1992, pp. 231–236.
doi:10.2514/3.46149